Supplemental Material can be found at:
http://www.jbc.org/content/suppl/2012/07/20/M112.384271.DC1.html

THE JOURNAL OF BIOLOGICAL CHEMISTRY VOL. 287, NO. 38, pp. 32254–32262, September 14, 2012
© 2012 by The American Society for Biochemistry and Molecular Biology, Inc. Published in the U.S.A.

High Conformational Stability of Secreted Eukaryotic Catalase-peroxidases

ANSWERS FROM FIRST CRYSTAL STRUCTURE AND UNFOLDING STUDIES[*] [S]

Received for publication, May 29, 2012, and in revised form, July 3, 2012 Published, JBC Papers in Press, July 20, 2012, DOI 10.1074/jbc.M112.384271

Marcel Zámocký[‡§], Queralt García-Fernández[¶], Bernhard Gasselhuber[‡], Christa Jakopitsch[‡], Paul G. Furtmüller[‡], Peter C. Loewen[‖], Ignacio Fita[¶], Christian Obinger[‡], and Xavi Carpena[¶1]

From the [‡]Department of Chemistry, Division of Biochemistry, BOKU, University of Natural Resources and Life Sciences, A-1190 Vienna, Austria, the [§]Laboratory of Molecular Microbiology, Institute of Molecular Biology, Slovak Academy of Sciences, SK-84551 Bratislava, Slovakia, the [¶]Institute for Research in Biomedicine (IRB Barcelona) and Institut de Biologia Molecular de Barcelona (IBMB) from Consell Superior d'Investigacions Científiques (CSIC), Parc Científic, 08028 Barcelona, Spain, and the [‖]Department of Microbiology, University of Manitoba, Winnipeg, Manitoba R3T 2N2, Canada

Background: Eukaryotic secreted KatGs are bifunctional enzymes extensively found in phytopathogenic fungi.
Results: Structural peculiarities, mainly in the N-terminal domain, dominate stability and other properties of eukaryotic secreted KatGs.
Conclusion: The distinctive requirements of secreted KatGs depend on very specific and fully conserved structural features.
Significance: This might be exploited to control plant fungal diseases that are jeopardizing food security worldwide.

Catalase-peroxidases (KatGs) are bifunctional heme enzymes widely spread in archaea, bacteria, and lower eukaryotes. Here we present the first crystal structure (1.55 Å resolution) of an eukaryotic KatG, the extracellular or secreted enzyme from the phytopathogenic fungus *Magnaporthe grisea*. The heme cavity of the homodimeric enzyme is similar to prokaryotic KatGs including the unique distal [+]Met-Tyr-Trp adduct (where the Trp is further modified by peroxidation) and its associated mobile arginine. The structure also revealed several conspicuous peculiarities that are fully conserved in all secreted eukaryotic KatGs. Peculiarities include the wrapping at the dimer interface of the N-terminal elongations from the two subunits and cysteine residues that cross-link the two subunits. Differential scanning calorimetry and temperature- and urea-mediated unfolding followed by UV-visible, circular dichroism, and fluorescence spectroscopy combined with site-directed mutagenesis demonstrated that secreted eukaryotic KatGs have a significantly higher conformational stability as well as a different unfolding pattern when compared with intracellular eukaryotic and prokaryotic catalase-peroxidases. We discuss these properties with respect to the structure as well as the postulated roles of this metalloenzyme in host-pathogen interactions.

Both aerobic and anaerobic organisms are exposed to internal and external reactive radical and nonradical oxygen species. The latter includes hydrogen peroxide (H_2O_2) that can be degraded by catalatic or peroxidatic pathways. In the catalatic pathway, two molecules of H_2O_2 are dismutated to water and dioxygen (Reaction 1), whereas in the peroxidatic pathway, hydrogen peroxide reduction follows Reaction 2 with AH_2 being a one-electron donor and $^{\bullet}AH$ being the corresponding radical.

$$2\ H_2O_2 \rightarrow 2\ H_2O + O_2$$
REACTION 1

$$H_2O_2 + 2\ AH_2 \rightarrow 2\ H_2O + 2\ ^{\bullet}AH$$
REACTION 2

Reaction 2 is catalyzed by a large diversity of heme and nonheme peroxidases (1–3). In contrast, Reaction 1 can be efficiently performed by only three families of enzymes: monofunctional manganese (nonheme) catalases, monofunctional heme catalases, and bifunctional heme catalase-peroxidases (KatGs),[2] which are unique because they are also able to perform the peroxidatic reaction (Reaction 2) at reasonable rates (4, 5).

Catalase-peroxidases are homodimeric oxidoreductases with each subunit being composed of N- and C-terminal domains with a close sequence and structural relationship with Class I peroxidases of the peroxidase-catalase superfamily (*e.g.* cytochrome *c* peroxidases, ascorbate peroxidases, and hybrid peroxidases of type A and B) (6). However, only the N-terminal domain of KatGs contains a heme cavity that is very similar to that of cytochrome *c* peroxidase and ascorbate peroxidases

* This work was supported by Grants BFU2009-09268 from Ministerio de Ciencia y Tecnologia (to I. F.), by Grant DG 9600 from the Natural Sciences and Engineering Research Council of Canada (to P. C. L.), and by the Canada Research Chair Program (to P. C. L.). The work was also supported by the Austrian Science Foundation - Fonds zur Förderung der Wissenschaftlichen Forschung (FWF) with doctoral program BioToP, Biomolecular Technology of Proteins, W1224 and the projects P20996 and P23855.
[S] This article contains supplemental Fig. 1.
The atomic coordinates and structure factors (code 3UT2) have been deposited in the Protein Data Bank, Research Collaboratory for Structural Bioinformatics, Rutgers University, New Brunswick, NJ (http://www.rcsb.org/).
[1] To whom correspondence should be addressed: Institute for Research in Biomedicine (IRB Barcelona) and Institut de Biologia Molecular de Barcelona (IBMB-CSIC), Parc Científic de Barcelona, Baldiri Reixac 10, 08028 Barcelona, Spain. Tel.: 34-93-4034956; Fax: 34-93-4034979; E-mail: xcvcri@ibmb.csic.es.

[2] The abbreviations used are: KatG, catalase-peroxidase; KatG1, intracellular or nonsecreted catalase-peroxidase; KatG2, extracellular or secreted catalase-peroxidase; MagKatG1, intracellular catalase-peroxidase from *M. grisea*; MagKatG2, extracellular catalase-peroxidase from *M. grisea*; BpKatG, catalase-peroxidase from *B. pseudomallei*; DSC, differential scanning calorimetry; Bis-Tris, 2-(bis(2-hydroxyethyl)amino)-2-(hydroxymethyl)-propane-1,3-diol.

Downloaded from www.jbc.org at University of Manitoba Libraries, on October 31, 2012

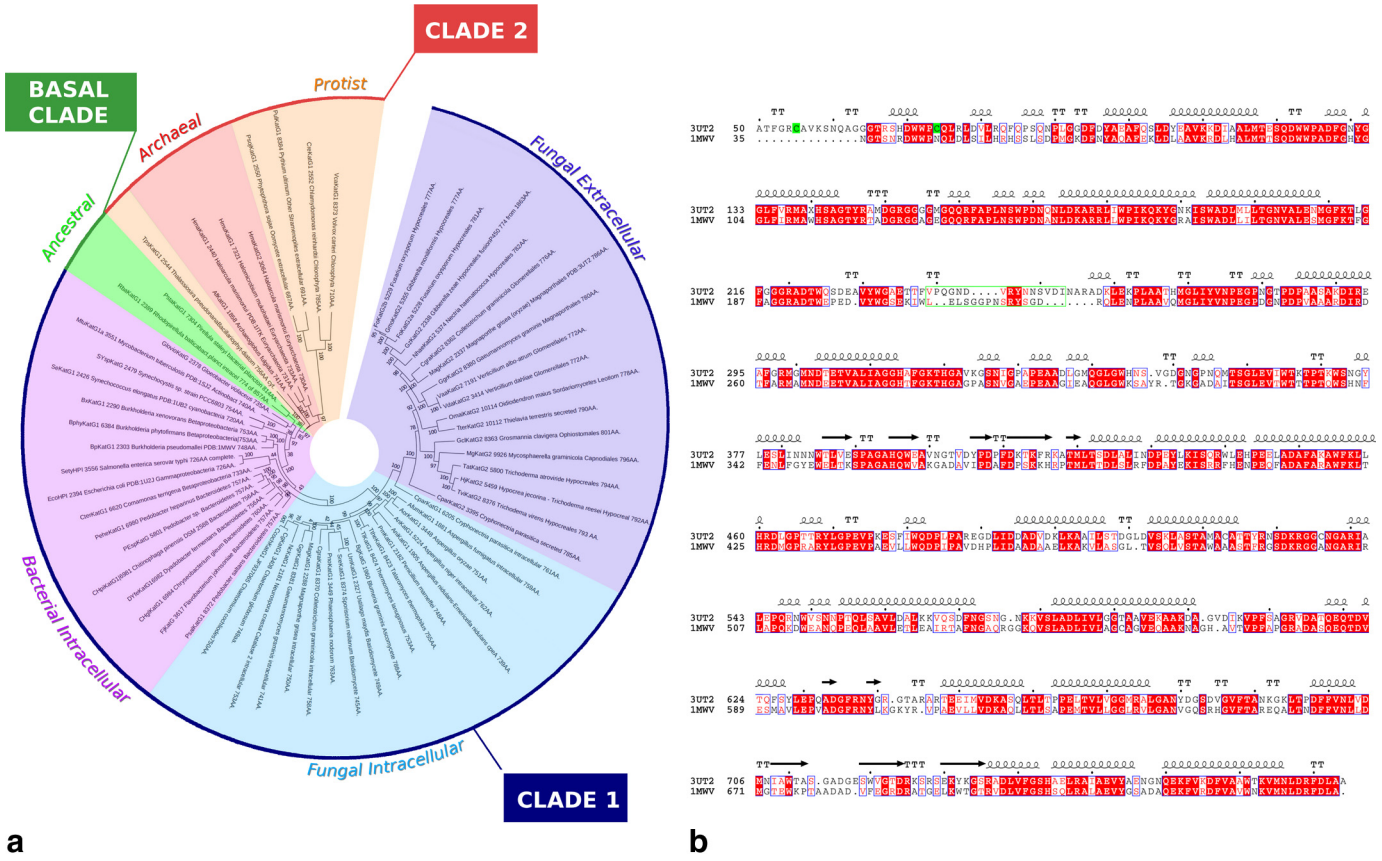

FIGURE 1. *a*, reconstructed phylogenetic tree showing prokaryotic KatGs and two well separated clades of eukaryotic catalase-peroxidases, namely a minor Clade 2 with protist KatGs and main Clade 1 with fungal KatGs consisting of the intracellular KatG1 and extracellular (secreted) KatG2 groups. Abbreviations of sequences and ID numbers correspond with PeroxiBase. The structures deposited in the PDB are also indicated. Molecular phylogeny was reconstructed using the maximum likelihood method of the MEGA 5.05 package (34). *b*, structural alignment of 3UT2 (MagKatG2) with 1MWV (BpKatG) was obtained using the structural similarity server of the European Bioinformatics Institute (EBI) (www.ebi.ac.uk) and manually reviewed after visual inspection (35). The major difference consists in the extended N terminus where two cysteine residues Cys-55 and Cys-74 (in *green*) cross-interact to produce two intersubunit disulfide bridges.

except for some crucial modifications required for the catalatic activity including the distal $^{+}$Met-Tyr-Trp adduct, which is formed post-translationally (5–9). The KatG-specific adduct participates in redox chemistry, and its reactivity appears to be regulated by a fully conserved mobile arginine that can adopt two pH-dependent conformations (10, 11). The unique catalytic properties of KatGs present a fascinating system in which to study how the protein framework can modulate catalysis at the heme center of heme enzymes.

Catalase-peroxidases are widespread in archaea and bacteria with about 40% of the bacteria possessing *katG* genes, often chaotically distributed among species (12). The catalase-peroxidase family, currently with 479 annotated sequences (PeroxiBase), is phylogenetically located at the origin of the peroxidase-catalase superfamily (6), formerly known as the superfamily of bacterial, fungal, and plant peroxidases, now containing over 6,700 annotated sequences. The superfamily most probably evolved from an ancestor of KatG, and phylogenetic reconstruction (Fig. 1*a*) suggests several lateral gene transfers (across the whole gene family) in addition to frequent duplication events (6, 12). Following the acquisition of *katG* genes by ancient ascomycete fungi via horizontal gene transfer from Bacteroidetes (1, 6), the evolution of eukaryotic KatGs proceeded toward the dominant Clade 1, whereas evolution of the mixed archaeal and protistan Clade 2 occurred in a different way (Fig. 1*a*). Currently, the nonsecreted or intracellular KatG1s are found in nonpathogenic and pathogenic fungi (13, 14), whereas the extracellular KatG2s or secreted KatG2s are found only in pathogenic fungi (15), suggesting that they are an important defense against the oxidative burst produced by infected plants (16–18).

During the last decade, KatGs from prokaryotes have been extensively investigated including the elucidation of the crystal structures of an archaeal and three bacterial enzymes (19–21). To date, only a small number of biochemical studies of eukaryotic fungal catalase-peroxidases have been reported, mainly focused on the intracellular KatG1 from *Neurospora crassa* (NcKatG1, originally named CAT-2) (22) and the rice blast fungus *Magnaporthe grisea* (MagKatG1) (14). Recently, the first biochemical data about the secreted KatG2 from *M. grisea* (MagKatG2) have been reported (15). Here we extend the characterization of MagKatG2 with the report of its crystal structure, the first of an eukaryotic catalase-peroxidase, at 1.55 Å resolution. It is similar in many respects to prokaryotic and archaebacterial KatGs but presents in addition a number of novel features that are fully conserved in secretory KatGs. These data are discussed with respect to the putative physiological role of secretory catalase-peroxidases in phytopathogenic

Downloaded from www.jbc.org at University of Manitoba Libraries, on October 31, 2012

organisms.

EXPERIMENTAL PROCEDURES

Heterologous Expression and Purification of MagKatG2—Recombinant catalase-peroxidases (wild-type MagKatG2 and single and double mutants) were expressed in *Escherichia coli* strain BL21 Star™ (DE3) (Invitrogen) and purified to homogeneity as described previously (15). Briefly, the inducible expression with 0.5% lactose overnight at 16 °C yielded on average 30 mg of soluble KatG2 per liter of M9ZL medium supplemented with hemin (75 μM final concentration). After homogenization by four ultrasonication cycles, the crude homogenate was centrifuged for 20 min at 45,000 × *g*, and the clear supernatant was loaded onto a 30-ml column of chelating Sepharose fast flow (GE Healthcare) charged with Ni^{2+} ions. His-tagged protein (with added protease inhibitors PMSF and leupeptin) was eluted with a linear gradient of 0–500 mM imidazole in 50 mM sodium phosphate, pH 7.5, 500 mM NaCl. Subsequent purification by hydroxyapatite column separated the high-spin heme fractions (15), which were pooled and concentrated with a Centriprep 50K (Millipore, for 30 min, 1,500 × *g*) and further purified by size exclusion chromatography (15). Dimeric protein fractions were concentrated up to 11 mg/ml in Centriprep 50K in 5 mM phosphate buffer, pH 7.5, and used for crystallization studies.

For protein electrophoresis, NuPAGE Novex Bis-Tris gradient gels (4–12%) or homogeneous 12% gels (Invitrogen) were used. Running buffer was MOPS-SDS, and the gels were stained with Coomassie Brilliant Blue (Sigma-Aldrich).

Design and Production of MagKatG2 Variants—Point mutations in the cloned *M. grisea katG2* gene were introduced with a PCR-based site-directed mutagenesis protocol using two complementary oligonucleotides with the planned mutation in the middle of their sequence. The PCR program included initial denaturation at 95 °C for 2 min, 16 cycles; 20 s at 98 °C, 1 min at 60 °C, 4 min at 72 °C; and a final amplification for 5 min at 72 °C (KAPAHifi DNA polymerase from PEQLAB Biotechnologie). Resulting DNA was cut with endonuclease DpnI (New England Biolabs) to remove the methylated, nonmutated DNA, and the purified mutated DNA was transformed into competent *E. coli* BL21-DE3-Star cells. Sequencing (LGC Genomics) confirmed the presence of only the planned mutation(s).

Design and Expression of Separated C-terminal Domain of MagKatG2—A DNA segment encoding the C-terminal domain of MagKatG2 was synthesized, codon-optimized for *E. coli* expression, at GenScript Inc. (Piscataway, NJ). The 944-bp-long NdeI-NotI region was cloned into pET21a (Novagen), and heterologous expression was achieved in M9ZL medium (15) under the same conditions used previously for MagKatG1 and MagKatG2 but without added hemin because the C-terminal domain does not bind heme. Purification to homogeneity succeeded under the same conditions as described for complete MagKatG2 (15), and the purified C-terminal domain of MagKatG2 was subjected to differential scanning calorimetry (DSC) and CD measurements as described below.

Protein Crystallization, Data Collection, and Structure Determination—Crystals of MagKatG2 were obtained using the sitting-drop vapor diffusion method at 4 °C with a protein concentration of 5 mg/ml in 5 mM phosphate buffer, pH 7.5. The mother liquor contained 15% PEG4000, 0.1 M sodium acetate, pH 4.6. At beam line ID23eh1 (European Synchrotron Radiation Facility (ESRF), Grenoble), diffraction data up to 1.55 Å were obtained using a flash-cooled crystal in a cryoprotectant solution, which contained an increased concentration of PEG4000 (35%). Data processed using the HKL package (23) corresponded to space group $P2_12_12_1$ with unit cell parameters a = 103.0 Å, b = 109.6 Å, c = 132.3 Å. Using MOLREP (24), a molecular replacement solution was found for MagKatG2 data using a monomer of KatG from *Burkholderia pseudomallei* (BpKatG) (1MWV) as a searching model. The protein structure was then refined at 1.55 Å resolution using REFMAC (25) and manually modeled with the molecular graphics program COOT (26), giving crystallographic agreement factors R and R_{free} of 19.3 and 22.5%, respectively (see Table 1). The solvent content (27) was of 47%, and a biological dimer was present in the asymmetric unit.

Differential Scanning Calorimetry—Thermal denaturation of MagKatG2 and its point mutants was monitored using DSC. All DSC measurements were performed on VP-DSC MicroCal LLC equipment from GE Healthcare. Protein concentration of all samples was either 5 μM or 10 μM. The temperature profile was recorded between 20 and 90 °C with a scan speed of 1 °C/min. The samples contained 0.5 M urea to avoid protein aggregation at higher temperatures. The results were evaluated and fitted with Origin 7.0 software (OriginLab).

Time-resolved UV-visible Spectroscopy—UV-visible spectra of recombinant KatGs were recorded with a Hitachi U-3900 spectrophotometer in the range 200–800 nm at 25 °C. The molar absorption coefficient of the ferric, high-spin MagKatG2 at Soret maximum ($\lambda_{404\,nm}$ = 102,600 M^{-1} cm^{-1}) was determined recently (15) and used for calculation of KatG concentrations throughout this work.

Apparent bimolecular rate constants of cyanide complex formation were determined by conventional stopped-flow spectroscopy (SX-18MV from Applied Photophysics, Leatherhead, UK) as described previously (15). Determination of the enzymatic parameters of the catalase activity was performed as described previously (14, 15).

Fluorescence and Electronic Circular Dichroism Spectroscopy—Unfolding of MagKatG2 by urea was followed by fluorescence spectroscopy using a Hitachi F-7000 fluorometer equipped with a thermostatic cell holder. A quartz cuvette of 10-mm path length was used to monitor changes of intrinsic tryptophan emission. The following parameters were used: excitation wavelength, 295 nm; emission wavelength range, 300–360 nm; excitation and emission bandwidth, 5 nm; photomultiplier tubes voltage, 400 V; scan speed, 60 nm/min. The final protein concentration for these measurements was 0.5 μM, and all samples prepared in 5 mM phosphate buffer, pH 7.0, were incubated with increasing concentrations of urea ranging from 0 to 8 M. After incubation for 18 h at 25 °C, the tryptophan emission spectra were recorded.

Electronic circular dichroism spectra were recorded on a Chirascan equipped with a thermostatically controlled cell holder (Applied Photophysics). For recording far-UV spectra, the quartz cuvette had a path length of 1 mm, and for recording

Downloaded from www.jbc.org at University of Manitoba Libraries, on October 31, 2012

visible spectra, a cuvette with a path length of 10 mm was used. To monitor the thermal unfolding, 5.8 μM KatG samples were incubated in 5 mM phosphate buffer, pH 7.0, containing 0.5 M urea (nondenaturing concentration (28)) with stepwise increasing temperature ranging from 20 to 90 °C. The instrument was flushed with nitrogen with a flow rate of 5 liters min^{-1}. The instrument allowed simultaneous UV/visible and electronic circular dichroism monitoring and was equipped with a Peltier element for temperature control. In the near-UV and visible region (250–500 nm), instrument parameters were set as follows: path length, 10 mm; spectral bandwidth, 1 nm; step size, 1 nm; scan time per point, 0.5 s (scan period, 25 μs × 20,000 counts); scan time, ~125 s. In addition, single wavelength scans were performed with the instrumental parameters set as follows: spectral bandwidth, 1 nm (Soret) or 0.5 (far-UV); scan time per point, 12 s; stepwise temperature increase (1 °C) with 2 min incubation time.

RESULTS AND DISCUSSION

Subunit Structure and Heme Cavity Architecture of Extracellular Catalase-peroxidase from M. grisea—Orthorhombic crystals of MagKatG2 confirm the dimeric structure common to KatGs with two subunits in the asymmetric unit. The electron density maps clearly define the main and side chains of residues Thr-51–Val-782 from the two subunits. The final model, which also includes two heme *b* groups and 1,616 water molecules, has crystallographic agreement R and R_{free} factors of 19.7 and 22.0% for 199,450 reflections at 1.55 Å resolution (Table 1). Both the structure of subunits as well as the organization in the molecular dimer are similar to prokaryotic KatGs (13–15) (Fig. 2. The superimposition of the subunits from MagKatG2 and BpKatG gives a low root mean square deviation of 1.15 Å for the Cα of 678 equivalent residues, and the value increases only slightly to a root mean square deviation of 1.35 Å for the superimposition of the dimers (Fig. 2*A*).)The structural similarity with the prokaryotic counterparts is evident by inspection of the heme cavity and the main access channel. The proximal (His-314/Trp-365/Asp-424) and distal (Arg-137/Trp-140/His-141) triads are found at almost identical positions, as is the KatG-typical covalent adduct $^{+}$Met-299-Tyr-273-Trp-140 (Fig. 2*B*). The existence of this post-translational modification in soluble MagKatG2 was demonstrated recently (15). It was interesting to see that Arg-461 (Fig. 2*B*), which has been postulated to act as a molecular switch modulating the redox properties of the $^{+}$Met-Tyr-Trp adduct (10), is present in only one conformation interacting with Tyr-273 (*i.e. Y*-conformation). This interaction suggests that the tyrosine must be unprotonated despite the low pH (4.6) of crystallization. In the published prokaryotic structures (10, 11, 19–21), this mobile arginine is found in two conformations (the *Y*- and *R*-conformations, with the latter pointing away from the adduct toward a conserved Arg (10, 11)) depending on the pH of crystallization and the oxidation state of the heme. Another structural feature that is correlated with the *Y*-conformation of the mobile arginine is a covalent modification of the indole nitrogen of the adduct tryptophan (10, 11). In the present structure, Trp-140 shows a peroxide modification with its second oxygen being 2.7 Å from the heme iron and also making a hydrogen bond with the catalytic His-141. In prokaryotic KatG structures, an alternative orientation of this modification pointing away from the catalytic His has been observed, although at higher pH values (10, 11).

TABLE 1
Data collection and structural refinement statistics for *M. grisea* KatG

Data collection statistics	
Space group	$P2_12_12_1$
Unit cell parameters *a, b, c* (Å)	103.0, 109.6, 132.3
Resolution (Å)	30-1.55 (1.61 1.55)[a]
Unique reflections	210461 (21066)
Completeness (%)	97.2 (98.4)
R_{sym}[b] (%)	11.4 (58.3)
$\langle I/\sigma I \rangle$	10.1 (2.4)
Redundancy	4.7 (4.0)
Model refinement statistics	
Resolution	20-1.55 (1.59 1.55)
No. of reflections	199450 (14321)
Free reflections	10526 (775)
R_{cryst}[c](%)	19.7 (32.4)
R_{free}[d](%)	22.0 (35.2)
No. of residues	1467
No. of waters	1616
No. of ligands	2
Average B-factor (Å^2)	
Protein	6.32
Ligands	8.31
Water	14.2
All atoms	7.31
r.m.s.[e] deviations	
Bond lengths (Å)	8.4×10^{-3}
Bond angles (°)	1.17

[a] The values in parentheses refer to statistics in the highest bin.
[b] $R_{sym} = \sum_{hkl}\sum_i |I_i(hkl) - \langle I(hkl)\rangle| / \sum_{hkl}\sum_i (hkl)$, where $I_i(hkl)$ is the intensity of an observation and $\langle I(hkl)\rangle$ is the mean value for its unique reflection; Summations are over all reflections.
[c] $R_{cryst} = \sum_h |F_o(h) - F_c(h)| / \sum_h |F_o(h)$, where F_o and F_c are the observed and calculated structure-factor amplitudes, respectively.
[d] R_{free} was calculated with 5% of the data excluded from the refinement.
[e] Root-mean square-deviation from ideal values.

The fact that the adduct Trp is chemically modified suggests that it participates in the H_2O_2 dismutation reaction of both prokaryotic and eukaryotic catalase-peroxidases. Freeze-quench EPR measurements combined with isotopic labeling on KatG from *Mycobacterium tuberculosis* have demonstrated that a radical on the $^{+}$Met-Tyr-Trp adduct is formed coincidentally with the *catalatic* reaction of KatG (8, 9). Moreover, it has also been demonstrated by hybrid quantum and molecular mechanics (QM/MM) calculations that the *Y*-conformation favors the formation of such an adduct radical (28). Differences in the relative proportions of *Y*- and *R*-conformations between prokaryotic KatGs and MagKatG2 with the latter having more *Y*-conformation at low pH are consistent with the lower pH optimum of the *catalatic* activity at pH 5.2 of MagKatG2 (15) when compared with 6.5 of BpKatG (20).

Distinctive Peculiarities of the MagKatG2 Structure—MagKatG2 presents, besides the clear similarities with prokaryotic KatGs, several new structural features that, importantly, seem to be common to all eukaryotic secreted KatG2s. These features include in particular (i) an N-terminal extension with a heme binding signal motif, (ii) two intersubunit disulfide bridges, and (iii) an insertion in the KatG-typical large loop 1 (LL1) (Figs. 1*b* and 2*A*). Interestingly, the binding for NAD^+ and ATP found in BpKatG occurs in this LL1 loop (29), suggesting that it might be a binding site for the as yet unknown physiological peroxidase substrates. As nonsecreted KatGs present the longest LL1 loop insertions (supplemental Fig. 1), it could be informative to

Downloaded from www.jbc.org at University of Manitoba Libraries, on October 31, 2012

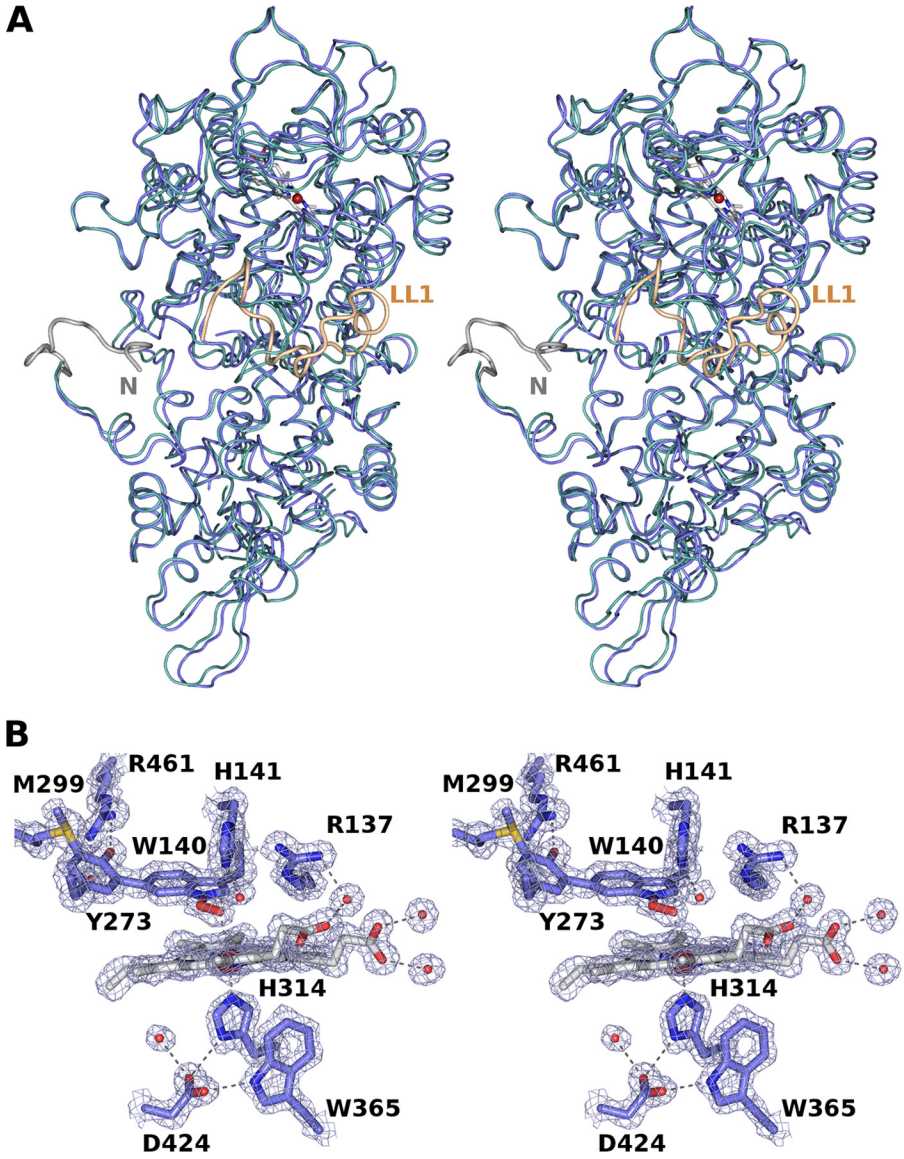

FIGURE 2. *A*, stereo view of the overall superposition of MagKatG and BpKatG monomers. The N-terminal extension of MagKatG is depicted in *gray*, whereas the LL1 loop has been highlighted in *pale brown*. The MagKatG N terminus protrudes to the same side as the heme access channel. *B*, stereo view of the active center, showing catalytic proximal and distal residues as well as the $^{+}$Met-Tyr-Trp covalent adduct and mobile arginine Arg-461. Trp-140, as already noted in other KatG structures, appears modified in its indole nitrogen as clearly seen in the electron density map.

determine for comparison a KatG1 structure. Loop LL1, despite its high variability, still requires the presence of an essentially fully conserved Arg-Tyr pair near the center of the loop (Fig. 3).

MagKatG2 contains more than 15 ordered residues at the N terminus when compared with the prokaryotic KatG structures (Fig. 1*b*). These extra residues in MagKatG2 wrap around the dimer two-fold axis, filling most of the cleft that exists between the two subunits in other KatGs (Fig. 3) (19–21). This arrangement still leaves a substantial disordered N-terminal region, not visible in the electron density maps, in MagKatG2 of about the same length as in the structures of bacterial KatGs (19–21). Most interestingly, in MagKatG2, two unique disulfide bridges between Cys-55 of one subunit and Cys-74 of the other, and *vice versa*, contribute to subunit intertwining (Fig. 3). Cys-55 and Cys-74 are fully conserved in all secretory KatG2s but not in other KatG clades, suggesting a possible physiological importance for this region.

Sequence alignments also reveal the presence of a conserved Cys-Pro (CP) (Cys-26–Pro-27 in MagKatG2) known as heme regulatory motif (30) in the flexible N-terminal region of Clade 1 but not Clade 2 KatGs (supplemental Fig. 1). This motif has been reported to transiently bind heme, *e.g.* during protein biosynthesis. However, mutational exchange of Cys-26 in MagKatG2 had no effect on heme occupancy in the corresponding recombinant variant (see below). Moreover, reports that this cysteine residue may participate in the formation of interchain disulfide bonds (cystines) (31) have not been corroborated in any crystal structures where this region is always disordered despite the possibility of subunit cross-linking. In fact, in the cytosol reducing environment, where all nonsecretable KatGs are localized, usually only very reactive cysteines form disulfide bridges.

High Thermal and Conformational Stability of MagKatG2—To probe the consequences of the intersubunit disulfide bridges in KatG2s, we investigated its thermal and conforma-

Downloaded from www.jbc.org at University of Manitoba Libraries, on October 31, 2012

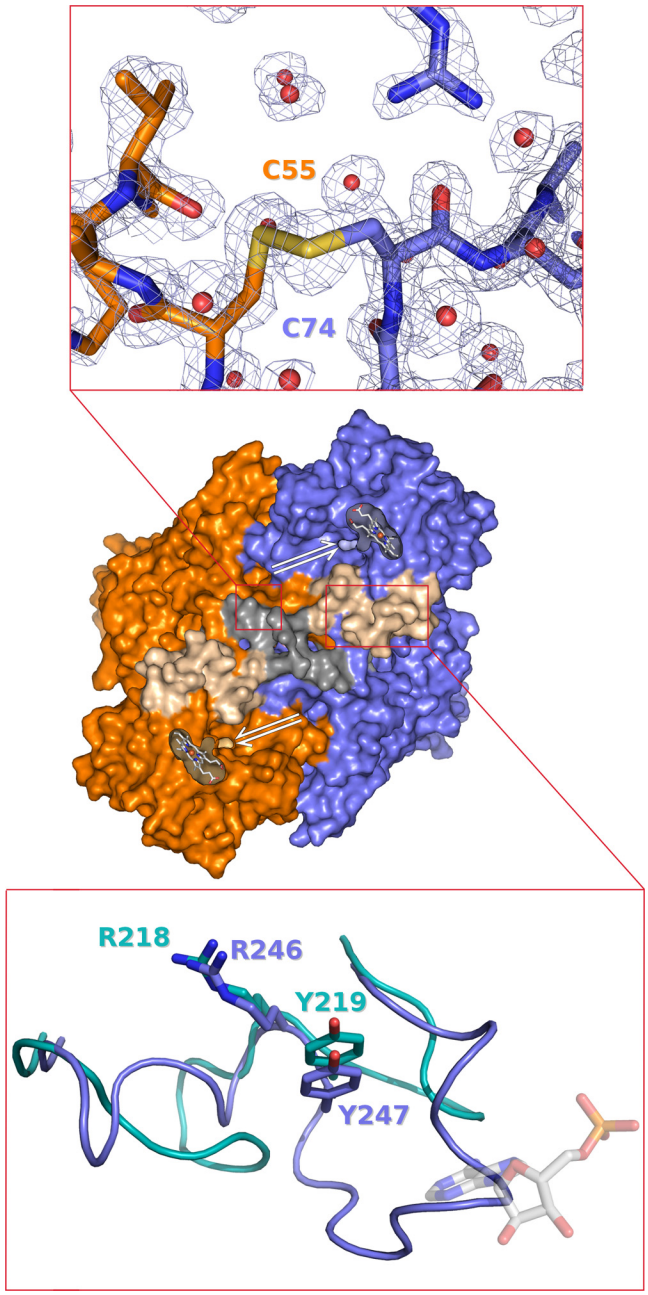

FIGURE 3. **Surface view of MagKatG2 dimer.** Subunits are depicted in different colors (subunit A, *blue*; subunit B, *orange*). In *dark gray*, the N-terminal extension when compared with prokaryotic KatG is depicted. A clipped view of the hemes of subunits A and B, the channel leading to them, as well as the heme cavity is shown in the *inset*. An electron density map showing Cys-55–Cys-74 disulfide bond is shown in the *upper inset*. The *lower inset* presents the superposition of LL1 from BpKatG (*turquoise*) and MagKatG2 (*blue*).

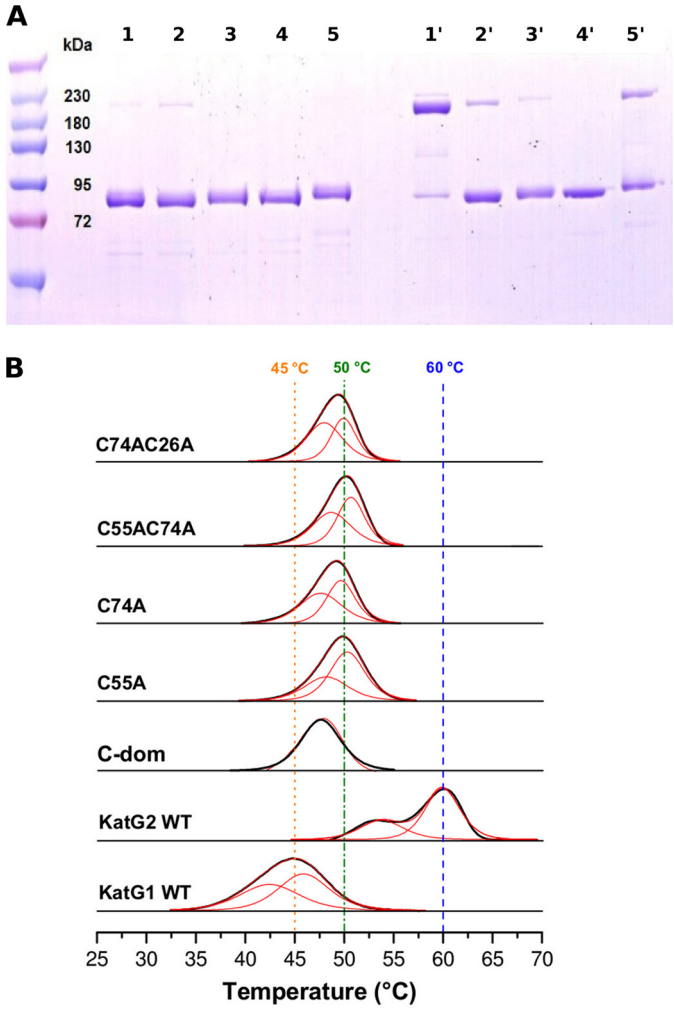

FIGURE 4. *A*, SDS-electrophoresis (12% NuPAGE, Invitrogen) of recombinant wild-type MagKatG2 and the variants C55A, C74A, C55A/C74A, and C26A/C74A, respectively, under reducing (*left*) and nonreducing (*right*) conditions. *Lanes 1* and *6*, wild-type MagKatG2; *lanes 2* and *7*, C55A; *lanes 3* and *8*, C74A; *lanes 4* and *9*, C55A/C74A; and *lanes 5* and *10*, C74A/C26A, respectively. *B*, differential scanning calorimetry of recombinant wild-type MagKatG2 and the variants C55A, C74A, C55A/C74A, and C26A/C74A. Also included is the thermogram of the intracellular catalase-peroxidase from *M. grisea* (MagKatG1) as well as the recombinant C-terminal domain of MagKatG2 (*C-dom*) (20). Base line-corrected thermograms (*bold lines*) were fitted using a non-two-state transition model. Conditions are as follows: 5 μM protein in 5 mM phosphate buffer, pH 7.5, and 0.5 M urea. In addition, the respective average melting temperatures are shown.

tional stability. We compared wild-type MagKatG2 with single mutants C55A and C74A as well as the double mutant C55A/C74A. Moreover, to test the possible roles of the cysteine in the CP motif, we also tested the C26A/C74A variant. The corresponding ferric high-spin proteins were heterologously expressed. All were dimeric in solution and showed a single band at ~85 kDa (theoretical molar mass of the monomer plus a heme and a His_6 tag is 85.30 kDa) in SDS-PAGE under reducing conditions (Fig. 4*A*). The Soret maxima were at 404–405 nm, and a purity number between 0.6 and 0.69 was obtained.

Under nonreducing conditions, wild-type MagKatG2 showed a prominent band that corresponded to the molar mass of a dimer, whereas the band at 85 kDa dominated for all other variants. These results confirm that the interchain disulfide bridges Cys-55–Cys-74 are present with a very high percentage in wild-type MagKatG2. In the variants, some minor bands at higher molar mass are still present as was also seen in previous investigations of archaeal and bacterial KatGs as well as intracellular eukaryotic KatGs (14, 19–21) that lack cysteines corresponding to Cys-55 and Cys-74. The band seen in the C26A/C74A variant could be explained by the formation of some symmetric (Cys-55–Cys-55) disulfide bond, which might be facilitated by the proximity of both residues to the molecular two-fold axis. It has to be mentioned that the large KatG from *Rhodopirellula baltica*, which is a member of the ancestral

Downloaded from www.jbc.org at University of Manitoba Libraries, on October 31, 2012

TABLE 2

Kinetic parameters of catalase activity followed polarographically by Clark-type electrode and cyanide binding followed by stopped-flow spectroscopy

The wild-type enzyme MagKatG2 and the four variants were investigated.

Kinetic parameter	Wild type	C55A	C74A	C55A/C74A	C74A/C26A
Catalase activity followed polarographically by Clark-type electrode					
K_m [mM]	3.84 ± 0.10	3.03 ± 0.17	3.66 ± 0.32	3.21 ± 0.44	3.52 ± 0.12
k_{cat} [s^{-1}]	6446 ± 182	6745 ± 275	7565 ± 458	6729 ± 670	7113 ± 170
k_{cat}/K_m [M^{-1} s^{-1}]	1.68×10^6	2.17×10^6	2.02×10^6	1.88×10^6	1.88×10^6
Cyanide binding followed by stopped-flow spectroscopy					
k_{on} [M^{-1} s^{-1}]	$(5.4 \pm 0.2) \times 10^5$	$(6.1 \pm 0.4) \times 10^5$	$(4.6 \pm 0.4) \times 10^5$	$(6.5 \pm 0.2) \times 10^5$	$(4.90 \pm 0.3) \times 10^5$

clade (supplemental Fig. 1) (6), has one additional cysteine residue in the N-terminal region (at positions that are not equivalent to Cys-55 or to Cys-74) in addition to the cysteine from the conserved heme regulatory motif.

Because the disulfide bridge Cys-55–Cys-74 covalently links the two N-terminal heme-containing domains of MagKatG2 and the flexible N-terminal region starts close to the molecular dimer interface where the main access channel is also located, it was important to probe whether exchange of conserved Cys-55 and/or Cys-74 has an impact on the catalytic properties of MagKatG2. Table 2 summarizes the data of these kinetic investigations. The steady-state kinetic parameters of the hydrogen peroxide dismutation reaction of wild-type MagKatG2 and all investigated variants were similar. Moreover, the kinetics of binding of the low-spin ligand cyanide to ferric iron (apparent k_{on} rates) as determined by stopped-flow spectroscopy was not influenced by manipulation of the KatG2-typical cysteines. The latter data also clearly underline that the accessibility to the heme cavity was wild type-like in all mutants.

Finally, we probed the impact of the KatG2-typical structural features on its thermal and conformational stability. When compared with both prokaryotic KatGs and eukaryotic intracellular KatG1s, KatG2 from *M. grisea* exhibits a significantly increased thermal stability. Differential scanning calorimetry (Fig. 4*B*) suggests that MagKatG2 follows a non-two-state unfolding with T_m values of the two transitions at 54 and 60 °C, respectively (Fig. 4*B*). By contrast, its intracellular counterpart (MagKatG1) shows an asymmetric endotherm that could also be fitted to a non-two-state transition with T_m values at 42 and 46 °C, respectively, very similar to prokaryotic catalase-peroxidases (32). Thermal unfolding analysis of the variants C55A, C74A, C55A/C74A, and C26A/C74A (Fig. 4*B*) indicates that disulfide bridges between Cys-55 and Cys-74 are responsible for the high structural integrity of KatG2. It also suggests that alternative cystines involving the cysteine from the CP motif cannot be formed in the absence of either Cys-55 or Cys-74, or at least do not contribute to the enhancement of stability.

In prokaryotic catalase-peroxidases, it has been demonstrated that during the first transition, mainly the N-terminal domain melted and heme was released, whereas the C-terminal (heme-free) domain mainly contributed to the second transition (32). To elucidate the sequence of unfolding of MagKatG2, we have expressed only its C-terminal domain (Fig. 4*B*) in *E. coli*. In contrast to the holoenzyme, it unfolds in a clear two-state transition with a T_m value at 47.5 °C, which corresponds to the first transition of the endotherms obtained for the single and double mutants (Fig. 4*B*). This suggests that in the secreted KatG2, the unfolding pathway is different when compared with other KatGs. To underline this assumption, we followed temperature-mediated unfolding additionally by electronic circular dichroism both at 208 nm (monitoring loss of ellipticity typical for α-helices) and at 412 nm (monitoring loss of ellipticity corresponding to heme *b* in its asymmetric environment at the active site). Loss of heme ellipticity started above 45 °C, but more than 80% was lost between 52 and 60 °C (Fig. 5*A*). In the denatured state, the prosthetic group was completely released (no remaining ellipticity at 412 nm). By contrast, loss of ellipticity at 208 nm already started above 40 °C, and there was a clear intermediate state, as was observed in the DSC experiments (both domains are mainly α-helical) (Fig. 5*B*) with the occurrence of residual ellipticity in the far-UV region in the unfolded state (Fig. 5*B*, *inset*), which has been observed with many other proteins including peroxidases. These findings support the hypothesis that in KatG2s, the N-terminal domain stabilized by intersubunit disulfide bridges is more stable than the C-terminal domain.

Finally, we observed that MagKatG2 is also more resistant to chemical denaturation (Fig. 5, *C* and *D*). Unfolding by urea results again in a non-two-step transition with a decrease of the heme Soret absorbance and blue-shift of the Soret maximum occurring in both transitions (c_{m1} = 3.8 M and c_{m2} = 7.1 M). However, the second transition shows a more pronounced decrease in both intensity (not shown) and shift of the Soret maximum, indicating that the N-terminal domain is more stable. Additionally, the change in the intrinsic fluorescence emission properties followed a clear non-two-state transition (c_{m1} = 4.1 M and c_{m2} = 7.1 M). The calculated conformational stabilities (ΔG°_{H2O}) of the individual domain were calculated to be 11–12 and 17–18 kJ/mol. These data clearly underline the high conformational stability of MagKatG2 when compared with prokaryotic or nonsecreted eukaryotic KatGs (32). In the latter, heme was already completely lost at 3 M urea during the first phase of unfolding ($\Delta G^\circ_{H2O} \sim 6.3$ kJ/mol) (32).

Conclusions—The first crystal structure of a eukaryotic catalase-peroxidase, solved at 1.55 Å resolution, reveals a high conservation of heme cavity and main access channel architecture including the unique KatG distal $^{+}$Met-Tyr-Trp adduct and the mobile arginine. Together with comparable catalytic properties, this conservation in structure suggests the same catalatic reaction mechanism in prokaryotic and eukaryotic KatGs including participation of the distal adduct with associated arginine in the hydrogen peroxide oxidation reaction. This

Downloaded from www.jbc.org at University of Manitoba Libraries, on October 31, 2012

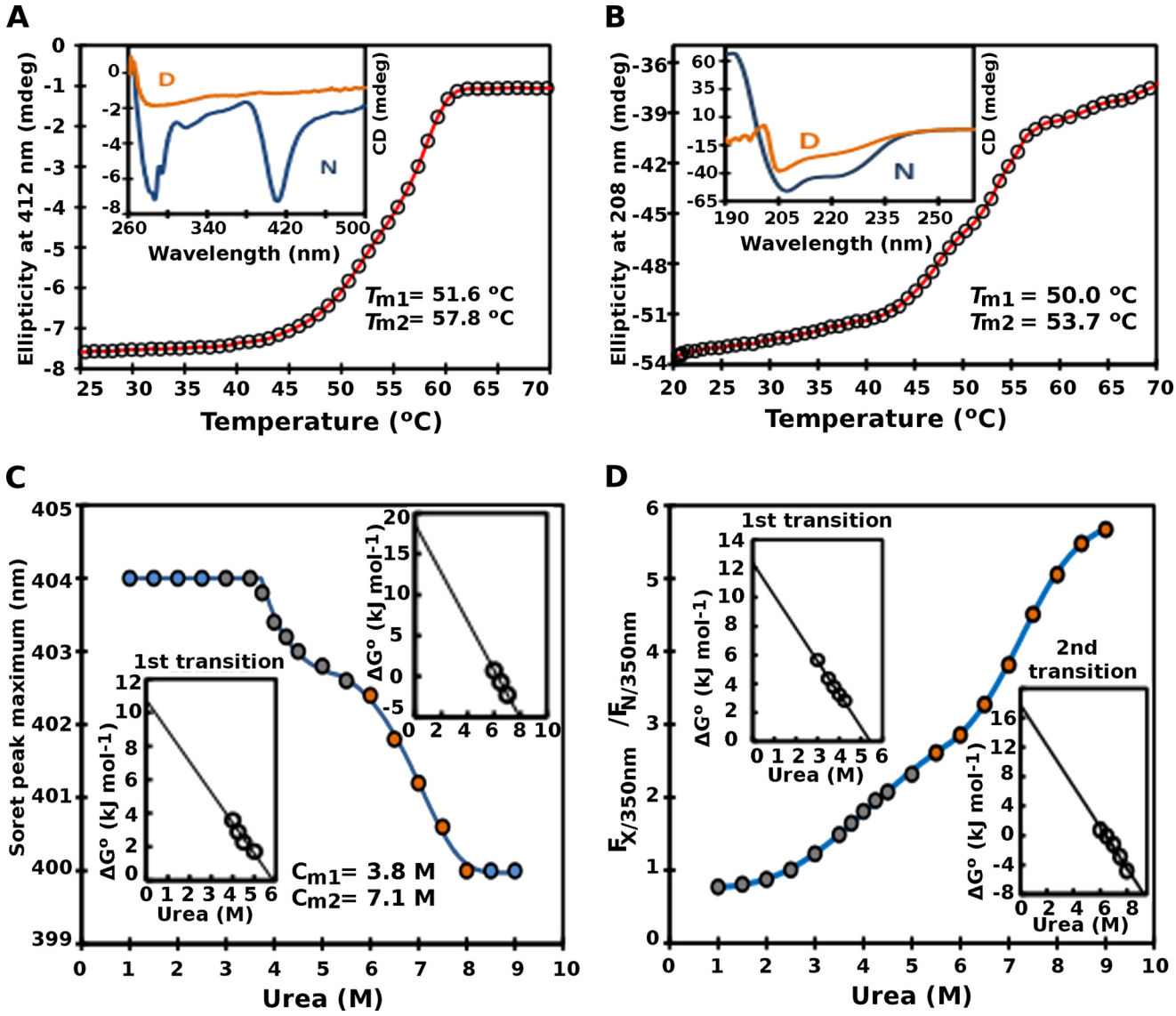

FIGURE 5. **Unfolding of wild-type catalase-peroxidase from *M. grisea* (MagKatG2) by temperature (*A* and *B*) and urea (*C* and *D*) at pH 7.0.** *A* and *B*, temperature-mediated unfolding followed by electronic circular dichroism at 412 nm (*A*) and 208 nm (*B*). *Insets* compare electronic circular dichroism spectra of native (*blue*) and denatured state (*orange*). *mdeg*, millidegrees. *C* and *D*, chemical denaturation by urea followed by UV-visible spectroscopy at Soret maximum (*C*) and by intrinsic tryptophan fluorescence (*D*). *Insets* show the change in standard free enthalpy with urea concentration.

assumption is also supported by the peroxide modification of the nitrogen of the adduct tryptophan.

It is significant that the residues responsible for the novel features found in the structure of MagKatG2 are fully conserved in all secreted KatG2s from phytopathogenic fungi. These features include the N-terminal extension and, most importantly, two novel disulfide bridges between the N-terminal domains of the two subunits of the homodimeric molecule. These modifications significantly increase the structural integrity of the enzyme as demonstrated by DSC, electronic circular dichroism, and fluorescence spectroscopy. Moreover, it renders the N-terminal domain to be more stable than the C-terminal domain, which is in contrast to all other so far investigated prokaryotic and eukaryotic representatives. Unfolding of the heme cavity either by temperature or denaturants requires more drastic conditions when compared with intracellular catalase-peroxidases. This should contribute to the structural integrity of the enzyme even under harsh extracellular conditions such as the ones resulting from the defense response of the plants. Ultimately, the peculiarities of KatG2 might be exploited as a target for control of the unprecedented number of fungal diseases that are jeopardizing food security (33).

REFERENCES

1. Zamocky, M., and Obinger, C. (2010). Molecular phylogeny of heme peroxidases. in *Biocatalysis Based on Heme Peroxidases* (Torres, E., and Ayala, M., eds), pp. 7–35, Springer, Berlin
2. Zamocky, M., Jakopitsch, C., Furtmüller, P. G., Dunand, C., and Obinger, C. (2008) The peroxidase-cyclooxygenase superfamily: reconstructed evolution of critical enzymes of the innate immune system. *Proteins* **72,** 589–605
3. Bernroitner, M., Zamocky, M., Furtmüller, P. G., Peschek, G. A., and Obinger, C. (2009) Occurrence, phylogeny, structure, and function of catalases and peroxidases in cyanobacteria. *J. Exp. Bot.* **60,** 423–440
4. Zamocky, M., Furtmüller, P. G., and Obinger, C. (2008) Evolution of catalases from bacteria to humans. *Antioxid. Redox Signal.* **10,** 1527–1548

Downloaded from www.jbc.org at University of Manitoba Libraries, on October 31, 2012

5. Smulevich, G., Jakopitsch, C., Droghetti, E., and Obinger, C. (2006) Probing the structure and bifunctionality of catalase-peroxidase (KatG). *J. Inorg. Biochem.* **100,** 568–585
6. Zámocký, M., Furtmüller, P. G., and Obinger, C. (2010) Evolution of structure and function of Class I peroxidases. *Arch. Biochem. Biophys.* **500,** 45–57
7. Vlasits, J., Jakopitsch, C., Bernroitner, M., Zamocky, M., Furtmüller, P. G., and Obinger, C. (2010) Mechanisms of catalase activity of heme peroxidases. *Arch. Biochem. Biophys.* **500,** 74–81
8. Suarez, J., Ranguelova, K., Jarzecki, A. A., Manzerova, J., Krymov, V., Zhao, X., Yu, S., Metlitsky, L., Gerfen, G. J., and Magliozzo, R. S. (2009) An oxyferrous heme/protein-based radical intermediate is catalytically competent in the catalase reaction of *Mycobacterium tuberculosis* catalase-peroxidase (KatG). *J. Biol. Chem.* **284,** 7017–7029
9. Zhao, X., Suarez, J., Khajo, A., Yu, S., Metlitsky, L., and Magliozzo, R. S. (2010) A radical on the Met-Tyr-Trp modification required for catalase activity in catalase-peroxidase is established by isotopic labeling and site-directed mutagenesis. *J. Am. Chem. Soc.* **132,** 8268–8269
10. Carpena, X., Wiseman, B., Deemagarn, T., Singh, R., Switala, J., Ivancich, A., Fita, I., and Loewen, P. (2005) A molecular switch and electronic circuit modulate catalase activity in catalase-peroxidases. *EMBO Rep.* **6,** 1156–1162
11. Carpena, X., Wiseman, B., Deemagarn, T., Herguedas, B., Ivancich, A., Singh, R., Loewen, P. C., and Fita, I. (2006) Roles for Arg-426 and Trp-111 in the modulation of NADH oxidase activity of the catalase-peroxidase KatG from *Burkholderia pseudomallei* inferred from pH-induced structural changes. *Biochemistry* **45,** 5171–5179
12. Passardi, F., Zamocky, M., Favet, J., Jakopitsch, C., Penel, C., Obinger, C., and Dunand, C. (2007) Phylogenetic distribution of catalase-peroxidases: are there patches of order in chaos? *Gene* **397,** 101–113
13. Zámocký, M., Furtmüller, P. G., and Obinger, C. (2009) Two distinct groups of fungal catalase/peroxidases. *Biochem. Soc. Trans.* **37,** 772–777
14. Zamocky, M., Furtmüller, P. G., Bellei, M., Battistuzzi, G., Stadlmann, J., Vlasits, J., and Obinger, C. (2009) Intracellular catalase/peroxidase from the phytopathogenic rice blast fungus *Magnaporthe grisea*: expression analysis and biochemical characterization of the recombinant protein. *Biochem. J.* **418,** 443–451
15. Zámocký, M., Droghetti, E., Bellei, M., Gasselhuber, B., Pabst, M., Furtmüller, P. G., Battistuzzi, G., Smulevich, G., and Obinger, C. (2012) Eukaryotic extracellular catalase-peroxidase from *Magnaporthe grisea*: biophysical/chemical characterization of the first representative from a novel phytopathogenic KatG group. *Biochimie* **94,** 673–683
16. Tanabe, S., Hayashi, N., Nishizawa, Y., Yamane, H., Shibuya, N., and Minami, E. (2008) Elicitor and catalase activity of conidia suspensions of various strains of *Magnaporthe grisea* in suspension-cultured cells of rice. *Biosci. Biotechnol. Biochem.* **72,** 889–892
17. Tanabe, S., Ishii-Minami, N., Saitoh, K., Otake, Y., Kaku, H., Shibuya, N., Nishizawa, Y., and Minami, E. (2011) The role of catalase-peroxidase secreted by *Magnaporthe oryzae* during early infection of rice cells. *Mol. Plant-Microbe Interact.* **24,** 163–171
18. Tanabe, S., Nishizawa, Y., and Minami, E. (2009) Effects of catalase on the accumulation of H_2O_2 in rice cells inoculated with rice blast fungus, *Magnaporthe oryzae*. *Physiologia. Plantarum.* **137,** 148–154
19. Yamada, Y., Fujiwara, T., Sato, T., Igarashi, N., and Tanaka, N. (2002) The 2.0 Å crystal structure of catalase-peroxidase from *Haloarcula marismortui*. *Nat. Struct. Biol.* **9,** 691–695
20. Carpena, X., Loprasert, S., Mongkolsuk, S., Switala, J., Loewen, P. C., and Fita, I. (2003) Catalase-peroxidase KatG of *Burkholderia pseudomallei* at 1.7 Å resolution. *J. Mol. Biol.* **327,** 475–489
21. Bertrand, T., Eady, N. A., Jones, J. N., Jesmin, Nagy, J. M., Jamart-Grégoire, B., Raven, E. L., and Brown, K. A. (2004) Crystal structure of *Mycobacterium tuberculosis* catalase-peroxidase. *J. Biol. Chem.* **279,** 38991–38999
22. Peraza, L., and Hansberg, W. (2002) *Neurospora crassa* catalases, singlet oxygen, and cell differentiation. *Biol. Chem.* **383,** 569–575
23. Otwinowski, Z., and Minor, W. (1997) in *Methods in Enzymology* (Carter, C. W., Jr., and Sweet, R. M., eds) Vol. **276,** part A, pp. 307–326, Academic Press, New York
24. Vagin, A. A., and Teplyakov, A.(1997) MOLREP: an automated program for molecular replacement. *J. Appl. Crystallogr.* **30,** 1022–1025
25. Murshudov, G. N., Vagin, A. A., and Dodson, E. J. (1997) Refinement of macromolecular structures by the maximum-likelihood method. *Acta Crystallogr. D Biol. Crystallogr.* **53,** 240–255
26. Emsley, P., and Cowtan, K. (2004) Coot: model-building tools for molecular graphics. *Acta Crystallogr. D Biol. Crystallogr.* **60,** 2126–2132
27. Collaborative Computational Project, Number 4 (1994) The CCP4 suite: programs for protein crystallography. *Acta Crystallogr. D Biol. Crystallogr.* **50,** 760–763
28. Vidossich, P., Alfonso-Prieto, M., Carpena, X., Loewen, P. C., Fita, I., and Rovira, C. (2007) Versatility of the electronic structure of compound I in catalase-peroxidases. *J. Am. Chem. Soc.* **129,** 13436–13446
29. Wiseman, B., Carpena, X., Feliz, M., Donald, L. J., Pons, M., Fita, I., and Loewen, P. C. (2010) Isonicotinic acid hydrazide conversion to isonicotinyl-NAD by catalase-peroxidases. *J. Biol. Chem.* **285,** 26662–26673
30. Zhang, L., and Guarente, L. (1995) Heme binds to a short sequence that serves a regulatory function in diverse proteins. *EMBO J.* **14,** 313–320
31. Saint-Joanis, B., Souchon, H., Wilming, M., Johnsson, K., Alzari, P. M., and Cole, S. T. (1999) Use of site-directed mutagenesis to probe the structure, function, and isoniazid activation of the catalase/peroxidase, KatG, from *Mycobacterium tuberculosis*. *Biochem. J.* **338,** 753–760
32. Banerjee, S., Zamocky, M., Furtmüller, P. G., and Obinger, C. (2010) Probing the two-domain structure of homodimeric prokaryotic and eukaryotic catalase-peroxidases. *Biochim. Biophys. Acta* **1804,** 2136–2145
33. Fisher, M. C., Henk, D. A., Briggs, C. J., Brownstein, J. S., Madoff, L. C., McCraw, S. L., and Gurr, S. J. (2012) Emerging fungal threats to animal, plant, and ecosystem health. *Nature* **484,** 186–194
34. Tamura, K., Peterson, D., Peterson, N., Stecher, G., Nei, M., and Kumar, S. (2011) MEGA5: molecular evolutionary genetics analysis using maximum likelihood, evolutionary distance, and maximum parsimony methods. *Mol. Biol. Evol.* **28,** 2731–2739
35. Gouet, P., Robert, X., and Courcelle, E. (2003) ESPript/ENDscript: Extracting and rendering sequence and 3D information from atomic structures of proteins. *Nucleic Acids Res.* **31,** 3320–3323

Downloaded from www.jbc.org at University of Manitoba Libraries, on October 31, 2012